

# THE SMALL-SCALE PHYSICAL AND CHEMICAL STRUCTURE OF EMBEDDED INTERMEDIATE MASS PROTOSTARS IN ORION

T.A. VAN KEMPEN<sup>1,2</sup>, S. LONGMORE<sup>3</sup>  
Center for Astrophysics, 60 Garden Street, Cambridge, MA 02138, United States

D. JOHNSTONE  
Herzberg Institute for Astronomy, Victoria, Canada and  
University of Victoria, Victoria, BC, Canada

A. FUENTE  
OAN, Madrid, Spain

T. PILLAI  
Caltech, Pasadena, CA, United States  
*Draft version August 18, 2010*

## ABSTRACT

Intermediate mass protostars form the bridge between the solar-like protostars that form the bulk of the field stars in our galaxy and the O and B stars that dominate the radiation fields within a galaxy. Although consistent theories exist for both ends of the mass range of stars, there is no encompassing continuous picture for the structure of protostars of all masses. Intermediate mass protostars, with luminosities between 50 and 5,000  $L_{\odot}$  and 3 to 10  $M_{\odot}$ . In this paper, results from an observing campaign at the Submillimeter Array targeting two intermediate mass protostars in Orion are presented. Intermediate mass (IM) protostars provide conditions that probe both LM protostars (hot corino's, nearby, disk presence) and HM protostars (clustering, strong UV/X-ray). The high resolution and bandwidth provided at the Submillimeter Array (SMA) allows one to study both the physical and chemical structure of IM protostars in detail. XXX conclusions XXX

*Subject headings:*

## 1. INTRODUCTION

Most studies of star formation concentrate on either low-mass (LM) or high-mass (HM) star-forming regions. LM star-forming regions have the advantage of being nearer, not being affected by strong radiation fields created by neighbouring (proto)stars and form in isolation and in an assumed monolithic collapse. However, the bulk of the field stars in our galaxy form in clusters where interactions from nearby more massive stars, stronger radiation fields and multiplicity form an important aspect of star formation (Adams & Myers 2001; Adams et al. 2006; Duchêne et al. 2007). As such, different evolutionary pictures have emerged for LM and HM star formation (Lada 1987; André et al. 1993; Robitaille et al. 2007; Fontani et al. 2009) and, even though some aspects in the two evolutionary pictures are similar (e.g. outflowing material, hot cores/corinos with chemical complexity/deuteration and the formation of protostellar disks in the later stages) no consistent star formation scheme covering protostars of all masses is agreed upon. Recent work from e.g. Keto & Zhang (2010), Longmore (2010) and Johnston et al. (2010) show that there may be large

similarities between individual HM and LM protostars. Even the presence of predicted high radiation pressure above  $M > 8M_{\odot}$  is mitigated by the physical structure and geometry, allowing O stars to form. The main differences are the clustering of LM protostars around HM protostars and thus the influence of the environmental radiation field, fragmentation of natal envelopes and the radiation field. A big unanswered question in cluster formation is whether HM protostars form first or LM do (See e.g. Vázquez-Semadeni et al. (2009) and the proceedings of the EPOS 2010 meeting<sup>4</sup> for discussion)

Intermediate mass (IM) protostars ( $(L_{\text{bol}} > 50$  and  $< 2,000)$  have not been studied in great detail. Although a few individual sources have been observed and analyzed (NGC 7129 IRS 2, Fuente et al. (2005a, 2007), IRAS 20050+2720, Beltrán et al. (2008)), it is uncertain if these are (i) typical of their class, (ii) typical for a larger spread in ages. However, IM protostars make excellent test-cases for star formation theory covering the full range of stellar masses. Being more luminous than LM protostars, they provide for larger warm zones within the enshrouding envelope in which complex chemistry may take place. Key molecular lines trace the structure of the inner envelope and outflow cavity walls. Recent observations (e.g. van Kempen et al. (2009b,a, 2010)) show that this structure is an important component for the heating

Electronic address: tvankempen@cfa.harvard.edu or tim.vankempen@gmail.com

<sup>1</sup> Alma Regional Center "Allegro", Leiden University, Leiden, the Netherlands

<sup>2</sup> Joined Alma Office, Santiago, Chile

<sup>3</sup> European Southern Observatory, Garching, Germany

<sup>4</sup> <http://www.mpia.de/homes/stein/EPoS/2010download.php>

and cooling balance and thus the evolution of protostars. Additionally, the proximity of IM protostars with typical distances less than 1.5 kpc also allows for studies at much smaller scales than HM protostars. Current generation submillimeter interferometers can reach resolutions  $<1''$ , essential in providing constraints for clustering by identifying individual members in fragmenting core.

XXX Longmore (2010) XXX

Lastly, chemistry is also more active than in low-mass sources (Fuente et al. 2005b), which can be used to constrain the amount and, more importantly, the influence of UV, both soft and far, of an accreting protostar and its corresponding outflow on the physical structure. A good tracer for chemistry are the complex organics and  $\text{CH}_3\text{CN}$ , as demonstrated by Bisschop et al. (2007) (High-mass survey) and Bisschop et al. (2008) (IRAS 16293-2422).

In this paper, we present recent results of observations of two intermediate mass protostars in Orion (D=450 pc), the closest cloud producing protostars more luminous than  $50 L_\odot$ . The two sources are not in the most crowded area, allowing one to more accurately probe individual sources. These two sources (NGC 2071 and L1641 S3 MM1) are thought to be representative of intermediate mass star formation in general. Both sources form in small, likely unbound clusters and are thought to create field stars in the galactic disks. As a comparison, results from Fuente et al. (2005b) and Fuente et al. (2007) on NGC 7129 FIRS 2 are used, as well as results from Bisschop et al. (2007), Bisschop et al. (2008) and Longmore (2010). In § 2, the observations are discussed, while the results are presented in § 3. § 4 analyses the data, while the structure in IM protostars are discussed in § 5. Finally, conclusions are presented in § 6.

## 2. OBSERVATIONS

Two sources were observed with the Submillimeter Array<sup>5</sup> over three nights in January/February 2010. The sources were selected based on the proposed sources within the Herschel Guaranteed Time key program WISH (Water in Star-forming region with Herschel<sup>6</sup> PI: E.F. van Dishoeck) of the intermediate mass protostars subprogram. These two sources, L1641 S3 MM1 and NGC 2071, are located in Orion, and as such the best IM protostars to study. The known properties of the sources can be found in Table 1.

### 2.1. SMA

The two sources were observed in two campaigns on the SMA in compact configuration and eSMA. Table 2 describes the settings that were used. Beam sizes, baseline lengths and correlator configuration are all presented. Data was taken first in compact configuration on 3<sup>rd</sup> and 4<sup>th</sup> January 2010. In a second campaign on February 11<sup>th</sup>, data was taken in the eSMA configuration. In the eSMA configuration<sup>7</sup> the SMA in very

<sup>5</sup> The Submillimeter Array is a joint project between the Smithsonian Astrophysical Observatory and the Academia Sinica Institute of Astronomy and Astrophysics and is funded by the Smithsonian Institution and the Academia Sinica.

<sup>6</sup> [www.strw.leidenuniv.nl/WISH](http://www.strw.leidenuniv.nl/WISH)

<sup>7</sup> The eSMA is a collaboration of the SMA, JCMT and CSO, to join the three facilities into a single sub-mm interferometer. For more information see <http://www.jach.hawaii.edu/JCMT/eSMA/>

extended configuration is combined to the James Clerk Maxwell Telescope (JCMT)<sup>8</sup> and the Caltech Submillimeter Observatory (CSO). For the compact configuration, instead of the normal 2 GHz correlator bandwidth, the new double-bandwidth mode was used. In this mode, 4 GHz is obtained in both the lower and upper sideband for a total of 8 GHz. The main lines that were targeted are  $^{12}\text{CO}$  2-1, set to chunk s13 (out of 48) of the upper sideband (USB), and the two well-studied isotopologues  $^{13}\text{CO}$  and  $\text{C}^{18}\text{O}$  in the lower sideband (LSB). The setting was chosen in such a way that a large number of additional lines were covered by the receivers, such as various  $\text{H}_2\text{CO}$  and  $\text{CH}_3\text{OH}$  lines, SO 5–4 and the methylcyanide ladder around 220.7 GHz. 3C454.3 was used as the bandpass calibrator for NGC 2071 and 3C273 for L1641 S3 MMS1 during the January tracks. For NGC 2071, the quasars 0501-019 and 3C120 were used as gain calibrators and Uranus as flux calibrator. A day later, when L1641 S3 MMS 1 was observed, the quasars 0607-085 and 0423-013 were used as gain calibrators, and Titan, which couldn't be used as Saturn was in the way, as flux calibrator. During the eSMA observations, correlator setup was limited to the 2 GHz bandwidth mode due to the increased number of antenna's. The limited time of 1.5 hours integration time was sufficient to cover a significant part of the UV-plane. 3c273 was used as bandpass and titan and vesta as flux calibrators. Due to the proximity to the source, vesta was also used as gain calibrator. The correlator was setup at 349 GHz, due to tracksharing with observations on Titan. Due to the limited time, only continuum observations are used. For all data reduction, a combination of the MIR package for IDL, the MIRIAD and CLASS software was used<sup>9</sup>. Cleaning was done to  $3\sigma$  using the Clark method in all images and spectra to obtain a natural weighting to reach the highest resolution.

### 2.2. Complementary data

Several other datasets are included in this paper as a complement. Using the SCUBA<sup>10</sup> archive (Di Francesco et al. 2008), data was obtained on NGC 2071. Since L 1641 S3 MMS 1 was not included in the archive due to its uncertain calibration. It was observed by SCUBA however. L1641 S3 MM1 data was retrieved from the CADZ archive in its uncalibrated state. Zavagno et al. (1997) previously observed L1641 S3 MMS 1 using the predecessor of SCUBA, the UKT14 common user bolometer instrument and reported a calibrated flux of 5.14 at 800  $\mu\text{m}$ . Using an interpolation of these UKT14 results and corrected for the observed source size, we adopt a flux of  $5+/-1$  Jy as a 'SCUBA' flux for L1641 S3 MMS1. Spitzer photometry of IRAC and MIPS 24 was obtained for all sources from the Spitzer archive (Megeath, priv. comm). This data taken within the scope of the Orion Spitzer program, led by Tom Megeath. See e.g. Guter-

<sup>8</sup> The JCMT is operated by The Joint Astronomy Centre on behalf of the Science and Technology Facilities Council of the United Kingdom, the Netherlands Organisation for Scientific Research, and the National Research Council of Canada.

<sup>9</sup> GILDAS is a software package developed by IRAM to reduce and analyze astronomical data. <http://www.iram.fr/IRAMFR/GILDAS>

<sup>10</sup> SCUBA was a continuum bolometer array operating at 450 and 850  $\mu\text{m}$  mounted on the JCMT

TABLE 1  
SOURCE PROPERTIES AND COMPLEMENTARY DATA

Source	R.A. hms	Dec. dms	$V_{\text{LSR}}$ $\text{km s}^{-1}$	$L_{\text{bol}}$ $L_{\odot}$	Dist. pc.
NGC 2071	05 47 04.7	+00 21 44	10.0	520	450
L1641 S3 MM1	05 39 55.9	-07 30 28	5.0	70	500

TABLE 2  
OBSERVATIONAL PARAMETERS.

Dates	Config.	Source	Beam size ("x")	Bandwidth GHz	Freq. GHz	Sideband	Band	Spectral res. $\text{km s}^{-1}$
Jan 3 2010	Compact	NGC 2071	4 GHz	230.538	USB	s13	128	
Jan 4 2010	Compact	L1641 S3 MMS1	4 GHz	230.538	USB	s13	128	
Feb 11 2010	eSMA	NGC 2071	2 GHz	349.415	USB	s17	128	

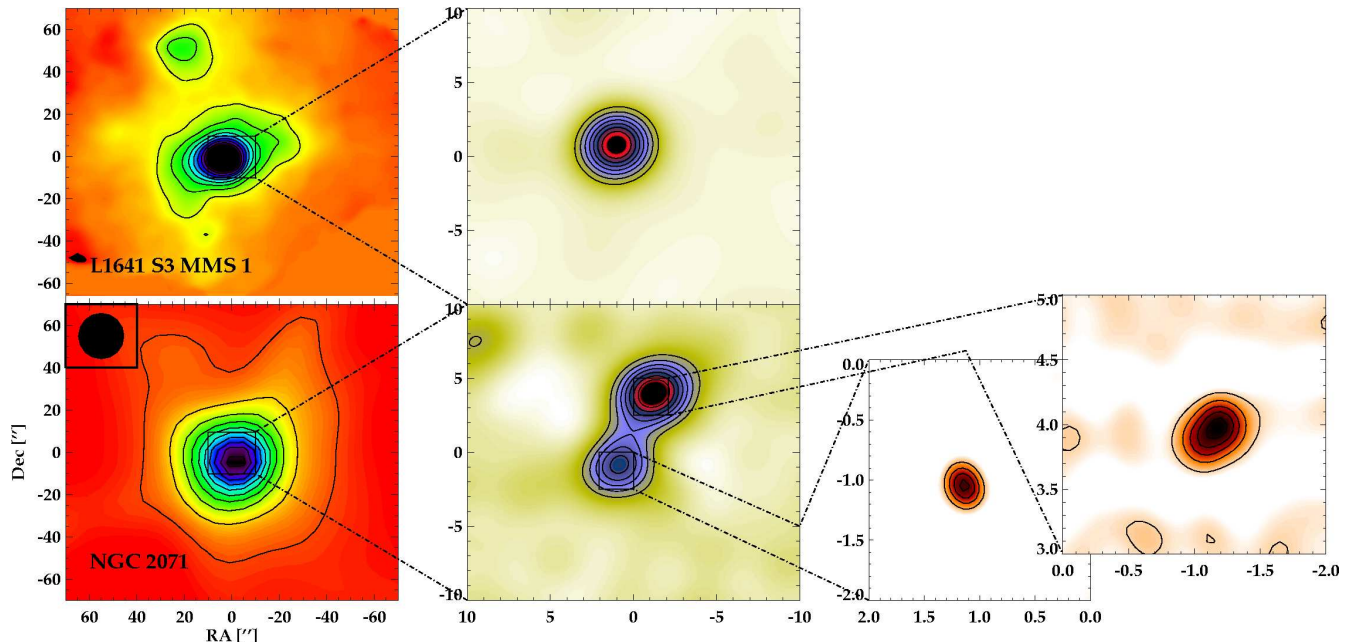


FIG. 1.— Comparison of continuum at different resolutions. First column shows the  $850 \mu\text{m}$  of SCUBA with a resolution of  $\sim 15''$ . Second column is SMA-compact  $1300 \mu\text{m}$  observations, with a resolution of  $\sim 4.5''$ . The third column shows very high resolution using eSMA (NGC 2071) and XXX at a resolution of  $0.3''$ . Contour lines are shown at 0.1, 0.2...  $0.9 \times$  the maximum of either source. XXX

muth et al. (2009) and Megeath, T. et al. (in prep) for more information on the Spitzer efforts in Orion Other photometric data points for the SED analysis were obtained from 2MASS archive.

### 3. CONTINUUM RESULTS

Fig. 1 shows the submillimeter continuum at different resolutions, ranging from  $15''$  to  $0.2''$ , using a combination of the  $850 \mu\text{m}$  and  $1.3 \text{ mm}$  data of SMA, eSMA and JCMT-SCUBA. Images are shown at three different length scales ( $120''$ ,  $20''$  and  $2''$ ). At each size scale, both images are normalized to the highest peak flux of either source, to accurately compare between the sources. Resulting fluxes from all these three scales can be found in Table 3.

#### 3.1. NGC 2071

TABLE 3  
RESULT OF THE CONTINUUM

Source	Core	Offset Jy/Beam	Peak Jy	Integrated Flux
SCUBA @ $850 \mu\text{m}$				
NGC 2071	-	-	-	21.9 +/- 0.05
L 1641 S3	-	-	5 +/- 1	30+/-2
Compact @ 230 GHz				
NGC 2071	A	4.2''	0.45	5.6
	B	1.4''	0.3	3.7
	C	12.2''	0.14	1.7
L1641 S3 MMS1		1.4''	0.42	5.2
eSMA @ 349 GHz				
NGC 2071	A	0.127	0.35	
	B	0.12	0.3	

<sup>1</sup> the beam goes down to about 50 AU.

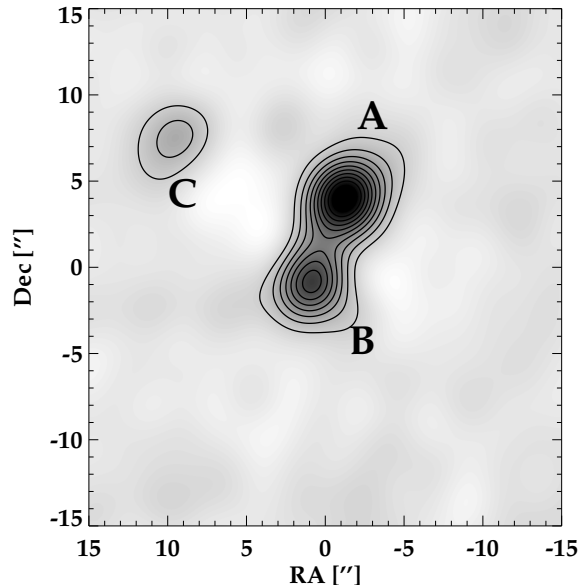


FIG. 2.— Zoom of the NGC 2071 protocluster at 230 GHz continuum. Contour lines are in 3,6,9..  $\sigma$ . Three cores are identified, labelled A, B, and C.

One can see that the two cores look very similar at scales of  $\sim 30''$ . Although we note that observational characteristics of SCUBA observations, as discussed in e.g. Di Francesco et al. (2008), may play a role, the peak flux is remarkably close. At higher resolutions using the SMA-compact observations, it is revealed that fragmentation is going on NGC 2071. It fragments into two peaks with possibly a third source in the north-east, as can be seen Fig. 2. At the highest resolutions available (eSMA at  $\sim 840 \mu\text{m}$ ), individual disks in the NGC 2071 sources are discerned in the A and B cores, from now on names 2071-A and 2071-B.

Fig. 3 shows the observed visibilities as a function of projected baseline, for the two cores identified as 2071-A and 2071-B, both in compact and eSMA configurations. It can be clearly seen that the profile for source A in compact config shows a resolved envelope, up until 20  $k\lambda$ , combined with an unresolved central source of 0.38 Jy (similar to Fig. 3 of Jørgensen et al. (2005)). Although source B is not as bright as source A, a similar fit can be reached in which an envelope is resolved up to  $\sim 30 k\lambda$ , with an unresolved central component of 0.15 Jy. eSMA observations confirm that these unresolved components are disks, as they are resolved on scales of a few hundred  $k\lambda$ , corresponding to  $\sim 200$  AU at the distance of Orion. The eSMA visibilities prove that the disks are resolved with radii of  $\sim 120$ -150 AU. The disks are both elongated, but clearly with different angles of their major axes. A central unresolved component is constrained to  $< 0.1$  Jy for both peaks.

**XXX Continuum models similar to models from Joergensen et al. 2007, Longmore et al. 2010 XXX**

Spitzer can provide important constraints on the individual sources. Images overplotting the SMA results onto the Spitzer-IRAC images, as well as Spitzer-IRAC and MIPS fluxes, can be found in Appendix A. 2071-B

and 2071-C are clearly detected in all bands, although 2071-B is dominated by emission at redder wavelengths. Source A, which is the brightest in the SMA images, is not seen in any band except weakly in the  $8 \mu\text{m}$  band and the  $24 \mu\text{m}$  MIPS. At the position of 2071-C a blue star-like source is seen in the Spitzer. XXX Does C have red excess XXX No disk-like component was detected down to a level of 10 mJy/beam in the eSMA observations for 2071-C. However, as this position was relatively far off the phase center and was in fact outside the dirty beam of JCMT and CSO, the presence of a disk, as suggested by SpitzerXX, cannot be ruled out. Analysis using a complete SED of all three sources is further done in § 4.1

### 3.2. L1641 S3 MM 1

In contrast to NGC 2071, Fig. 1 reveals that L1641 S3 MM 1 is not fragmenting into multiple sources at smaller scales. Only a single continuum source is seen at this size scale. The 1.3 mm continuum with the SMA-compact shows an almost perfectly spherical source. XXX extended/VEX?? XXX.

The visibilities (see Fig. 4) confirm that the envelope is resolved and structure variations are extending inwards to 60  $k\lambda$ , another difference with NGC 2071. No unresolved component is dominating between 20 and 60  $k\lambda$  of the projected baselines. Any unresolved component that could correspond to a central disk is limited to 0.15 Jy at scales smaller than 1,000 AU. This is almost three times smaller than seen in 2071-A and twice as small as 2071-B and twice as small as the disk components resolved in the eSMA.

The Spitzer images for L1641 S3 MMS 1 in appendix A shows that the embedded source is related to the greenest in the picture, dominated by an outflow traced as a 'green fuzzy'. Other members in the L1641 protocluster can be seen, but none emit at 1.3 mm wavelengths. ? classifies these sources as XXX.

## 4. CONTINUUM ANALYSIS

### 4.1. SED

A powerful tool in the analysis is the Spectral Energy Distribution. Studies such as Robitaille et al. (2007) and Evans et al. (2009) have very efficiently used large databases of 2Mass and Spitzer observations to characterize large number of sources using their SEDs. Although some studies such as Crapsi et al. (2008), Enoch et al. (2008) and van Kempen et al. (2008) show that SEDs are not a definitive answer, it does allow for a good first-look into the evolutionary stage and physical structure of a protostar. Using the Spitzer (see Appendix A) and submm photometry of both SMA and JCMT, complemented by 2MASS where available, SEDs were constructed for all four sources (2071-A,B and C and L1641 S3 MMS 1) and in turn fitted with the SED grid of models as detailed by Robitaille et al. (2006) using the online SED fitter<sup>11</sup> (Robitaille et al. 2007). Although this fitter is not accurate to determine masses, it gives a good first approximation. Fig 4.1 gives the fitted SED of 2071-A, 2071-B and 2071-C. Table 4.1 gives the resulting envelope masses, bolometric luminosities, stellar masses and

<sup>11</sup> The SED fitter can be found at <http://caravan.astro.wisc.edu/protostars/>

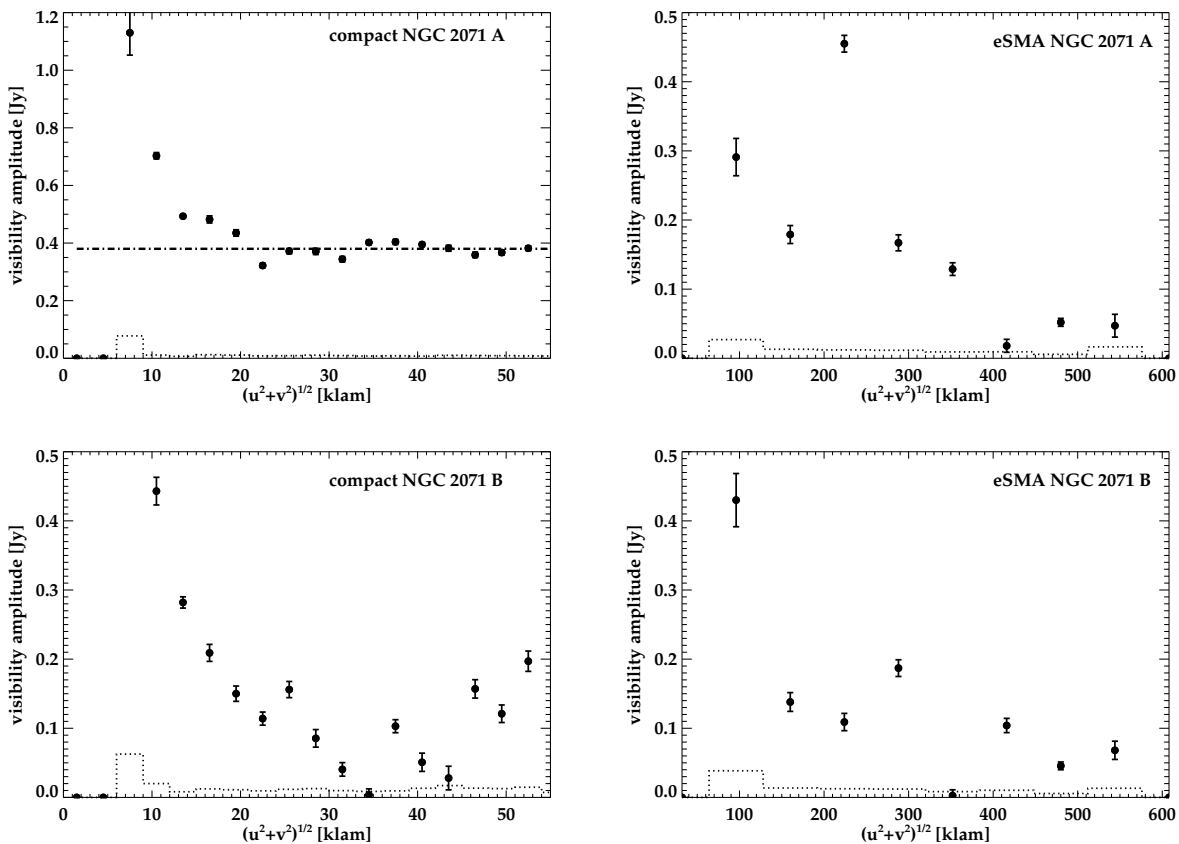


FIG. 3.— Observed continuum visibility amplitudes of Table XXX as a function of the projected baseline length for NGC 2071 A and B. Error bars are  $1\sigma$  statistical errors and the dotted histogram indicates the zero-expectation level. *Upper row* The compact configuration data of sources A (*left*) and B (*right*). Data clearly indicates a classical profile as seen in e.g. Fig. 3 of Jørgensen et al. (2005) where a resolved envelope transitions into an unresolved disk-like component. In the figure for source A in compact configuration this is indicated by the horizontal line. *Lower row* The eSMA data at the same position. Here it can be clearly seen that the disks are resolved and visibilities fall off until a  $k\lambda$  of  $\sim 500$  which is about XXX AU.

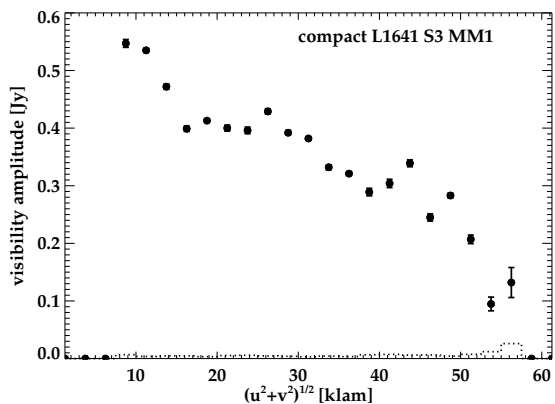


FIG. 4.— Observed continuum visibility amplitudes of Table XXX as a function of the projected baseline length for L1641 S3 MM1. Error bars are  $1\sigma$  statistical errors and the dotted histogram indicates the zero-expectation level.

the ratio of envelope over stellar mass of the SED, derived by averaging the 10 best fits.

In Table 4.1 it can be seen that the luminosities together by far do not account for the luminosity of 520, assumed for the total core. Most of that high core lumi-

nosity of earlier results is due to the inclusion of IRAS 60 and 100  $\mu\text{m}$  photometry, which often includes a significant contribution from the ISM and material surrounding the core. Higher resolution imaging using the PACS and SPIRE instruments on Herschel, as proposed by HOPS (PI: T. Megeath) will observe these regions and determine more accurate core luminosities.

Envelope masses found range from a few solar masses for 2071-C to almost  $15 M_{\odot}$  for 2071-B. This is significantly higher than the masses commonly found in nearby clouds, which are typically a few tens to  $\sim 2 M_{\odot}$  (Shirley et al. 2000). Although the Robitaille SED fitter can be used to determine limits on the disk emission, the high  $A_V$  and increasing optical depth of the dust makes this very uncertain and are thus omitted from this work. We also derived estimates on the stellar masses. From this it can be seen that the L1641 S3 MMS 1 internal source is significantly more massive ( $3.5 M_{\odot}$ ) than any of those in the NGC 2071 minicluster ( $< 1 M_{\odot}$ ) and that the ratio of envelope over stellar mass is much lower. This could be indicative that L1641 S3 MMS 1 is more evolved than the NGC 2071 cluster. This has a significant influence on the radiation field produced by the star at UV wavelengths XXX accretion rate XXX In § 5 we discuss the role of fragmentation and age more in-depth.

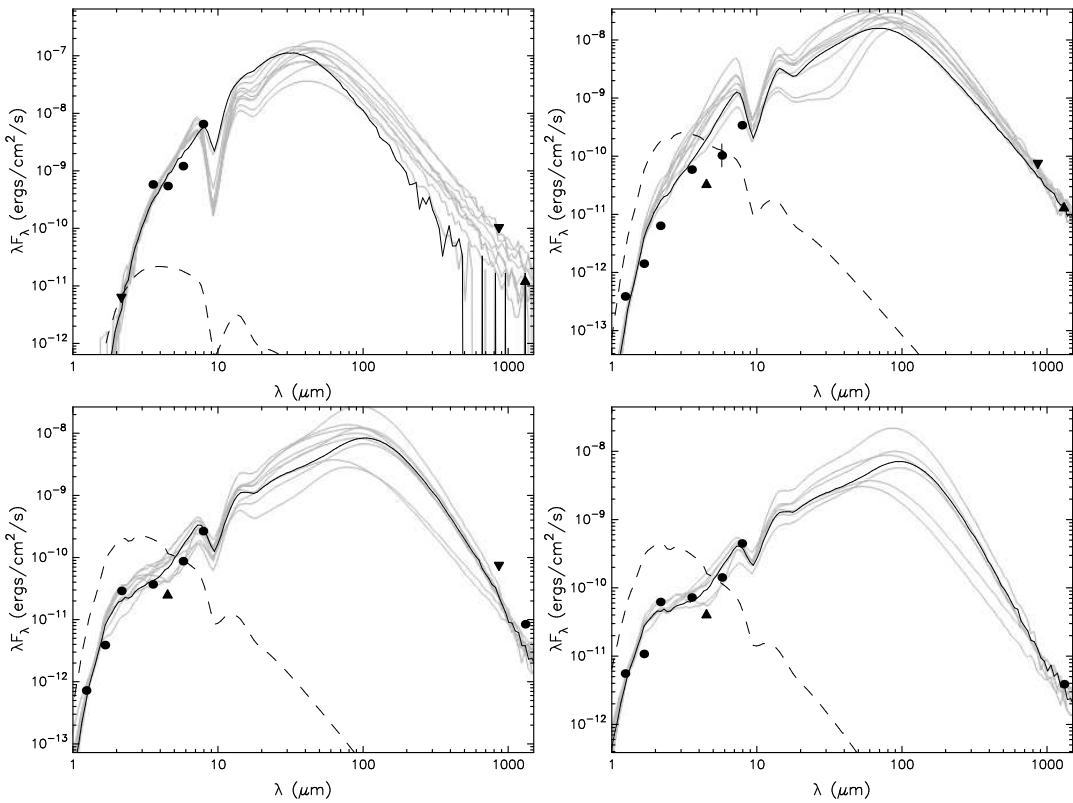


FIG. 5.— *Top row*: SED fits of L1641 S3 MMS 1 and the A core of 2071. *Bottom row*: the SED fits of the B and C cores in 2071.

TABLE 4  
RESULTS FROM ROBITAILE SED FIT<sup>a</sup>

Source	L <sub>bol</sub> L <sub>⊙</sub>	Env. Mass M <sub>⊙</sub>	Stellar Mass	T <sub>bol</sub>	α <sub>IR</sub>	M <sub>env</sub> /M <sub>star</sub>
2071-A	<27	8.2	0.9			30
2071-B	10	14.2	0.5			20
2071-C	3.4	~3.5	0.5			6.8
L1641 S3 MMS 1	250	>9.6	>3.5			2.7

<sup>a</sup> results from the 10 best-fitting models after by-eye inspection are averaged. The spread in these values is about 50% from the given value. A<sub>V</sub> values range from 5 - 35 and are the main cause for this large error.

#### 4.2. Dust characteristics

If one assumes dust properties of Ossenkopf & Henning (1994), also known as OH5 dust, one can derive the masses at each scale using the following formula.

$$M_D = S_\nu D^2 / B_\nu(T_{dust}) \kappa_\nu \quad (1)$$

where  $S_\nu$  is the integrated flux density,  $B_\nu(T_{dust})$  the Planck function at temperature of  $T_{dust}$ ,  $\kappa_\nu$  the opacity per gm of gas and dust. It is assumed that at both 1.3 mm and 850  $\mu$ m the dust is optically thin.  $\kappa_\nu$  is 0.02 cm<sup>2</sup> gm<sup>-1</sup> at 850  $\mu$ m and 0.009 cm<sup>2</sup> gm<sup>-1</sup> at 1.3 mm. Table 4.2 shows the calculated masses. A free parameter however is the temperature. At large scales, the mass is dominated by the cold dust and oft assumed to be 20 K (Shirley et al. 2000). This temperature is also adopted in this paper. The disks at smaller scales, as traced by the eSMA, where the density is often much higher, are also assumed to be cold and 20 K, due to the self-shielding.

Masses can be computed with a lower dust tempera-

TABLE 5  
MASS ESTIMATES

Source	Core	15''	4'' <sup>a</sup>	0.25''
		Mass [M <sub>⊙</sub> ]		
NGC 2071	A	21.7 <sup>b</sup>	12.3	0.35
	B	21.7 <sup>b</sup>	8.2	0.29
	C	21.7 <sup>b</sup>	3.7	<0.2
L1641 S3 MMS1		20.9	11.46	

<sup>a</sup> Observations taken at 230 GHz with dust opacity  $\kappa=0.009$ . See text.

<sup>b</sup> Single core

ture, e.g. 10 K, and are generally higher by a factor 3. If the temperature is higher, e.g. 40 K, the amount of material needed is lower and masses should be adjusted similarly to a factor 2.5 lower than those given in 4.2. However, estimates of  $\kappa_\nu$  can vary by at least a factor 3. For more discussion on temperature variations and dust properties, see Shirley et al. (2000), van der Tak et al.

(1999) and Ossenkopf & Henning (1994).

In general, the masses are dominated by the envelopes, as seen from the SED fitting. Only small amounts ( $<0.5 M_{\odot}$ ) are not resolved out at the highest resolutions with the eSMA. Even if a large amount, e.g. 75%, of the disk material is resolved out by the lack of shorter baselines, disk masses would still be below  $2 M_{\odot}$ , with the envelope contained factors of at least 4 more mass than the disk from the SMA-compact observations, in which the contributions of the cloud are resolved out. However, a scenario in which the disks are largely resolved out is unlikely, since at the distance of Orion of 450 pc, the resolved disks in the eSMA observations are still 120-200 AU in radius. In conclusion, both sources, despite their infra-red detections with Spitzer (see Appendix) are clearly deeply embedded sources equivalent to the Stage 0.

Masses derived from the dust emission agrees with the masses found by the SED fitting, if one takes the different scales at which masses were calculated into account. The SED masses are slightly lower than the masses derived for the  $15''$  scale, but agree very well with those at  $4''$ . As the physical scale of  $4''$  at a distance of Orion corresponds to  $\sim 25''$  at distances of nearby clouds such as Taurus and Ophiuchus, it isn't unreasonable to claim that the SMA-Compact observations are good tracers of the actual protostellar envelopes. The total of mass at  $4''$  of the three components of 2071 equals 24.2, within the estimated error of 20% of the mass calculated using the SCUBA flux.

#### 4.3. The fragmentation of NGC 2071

One of the important goals of this paper is to discern the influence of fragmentation and why and how fragmentation, assumed to be thermal, took place in the NGC 2071 mini-cluster, but why no fragmentation occurred in L1641 S3 MMS 1. In Longmore (2010) a method to quantify the fragmentation is introduced for the high-mass protocluster G8.68-0.36, which we adopt and adapt here for the NGC 2071 SMA observations. It has been adapted for low- and intermediate masses instead higher masses as no generation of low-mass sources is present, as was assumed in Longmore (2010).

In this simplistic scenario, at  $t = t_0$ , the original "supercore", now called core ABC, is similar to a large protostellar core or a small IRDC. We therefore assume equivalent characteristics:  $T_0 = 20$  K and  $n_0 = 10^4 \text{ cm}^{-3}$  **XXX needs ref from both mass sides! is quite important XXX.**

If one in turn assumes isothermal collapse, the main variable to rise is the density,  $n$ . At certain times later, defined as  $t = t_{\text{frag},1}$  and  $t = t_{\text{frag},2}$ , thermal fragmentation takes place between cores A,B and C, with  $T_{\text{frag},x}$  and  $n_{\text{frag},x}$ . Note that the model allows  $t_{\text{frag},1} = t_{\text{frag},2}$ . At an even later time,  $t = t_{\text{now}}$ , we observe the mini-cluster with masses  $M_{\text{now}}$  for A,B and C and distances  $\Lambda_{\text{now}}$  AB, AC, and BC. These observational results are in turn used to infer the physical conditions at  $t_{\text{frag},1}$  and  $t_{\text{frag},2}$  and determine if  $t_{\text{frag},1} = t_{\text{frag},2}$  or not. For this, the Jeans mass and length are used, written in a form to be related to  $T$  and  $n$ .

$$M_J = 1 M_{\odot} \left( \frac{T}{10\text{K}} \right)^{\frac{3}{2}} \left( \frac{n}{10^4 \text{cm}^{-3}} \right)^{-\frac{1}{2}} (2)$$

and

$$\Lambda_J = 0.1 \text{ pc} \left( \frac{T}{10\text{K}} \right)^{\frac{1}{2}} \left( \frac{n}{10^4 \text{cm}^{-3}} \right)^{-\frac{1}{2}} (3)$$

These equations were solved and  $T_{\text{frag}}$  and  $n_{\text{frag}}$  were derived for each combination of A,B and C in several scenario's. In these scenario's, conclusions of the last scenario were used to construct subsequent scenario. A problem here are the masses. First, we have to account for stellar mass, so we use  $M_{\text{total}}$  and not  $M_{\text{env}}$ . Second, the A and B cores are much heavier. Unless noted otherwise we take the lowest mass of each core and assume excess mass of the other core has a different origin, likely accretion at a later stage. A calculation of a fragmentation of unequal masses is considered to be beyond the scope of this paper. But we will discuss this in section § 5.X, where caveats are discussed.

##### 4.3.1. Scenario I: Isothermal ( $T=20$ K) collapse, $t_{\text{frag},1} = t_{\text{frag},2}$ , $M_{\text{now}} = M_{\text{frag},x}$ and $\Lambda_{\text{now}} = \Lambda_{\text{frag},x}$

In an isothermal collapse of 20 K, equations above reduce to  $M = 250 \times n_{\text{frag}}^{-0.5}$  and  $\Lambda = 141 \times n_{\text{frag}}^{-0.5}$ . If we then calculate the densities, using the masses and lengths, the densities vary wildly, ranging from a few times  $10^5$  for the calculation using the jeans length and  $10^3$  for jeans mass. In addition, the densities of AB versus AC and BC are very different and vary with a factor 7 to 10. It is very clear that  $n_{\text{frag}}$  for each combination of cores as calculated from mass and distance is not physical. The very low densities of these masses are unrealistic and even below densities commonly observed in e.g. IRDCs or protostellar cores (?).

##### 4.3.2. Scenario II: Isothermal ( $T=20$ K) collapse, $t_{\text{frag},1} = t_{\text{frag},2}$ and $\Lambda_{\text{now}} = \Lambda_{\text{frag},x}$ , but $M_{\text{now}} \neq M_{\text{frag},x}$

A likely possibility is that although fragmentation occurred early, but the bulk of the mass was still located at much larger distances. This is likely as we still see material in the SCUBA images at distances of 10,000 AU and greater. Each fragment still accretes after  $t_{\text{frag}}$  from a global accretion of the large-scale supercore. In this scenario we in turn use the densities of  $\sim 10^5$  from the distance calculation to derive a  $M_{\text{frag}}$  for each core. Masses of  $0.35 M_{\odot}$  for A and B and  $0.7 M_{\odot}$  for core C are found. The fact that the masses of A+B equals C is immediately apparent and should be noted. This is much lower than the current mass of each core. One can imagine that a fragmentation event happened in which core ABC fragmented into core AB and C.

##### 4.3.3. Scenario III: Isothermal ( $T=20$ K) collapse, $\Lambda_{\text{now}} = \Lambda_{\text{frag},x}$ , $t_{\text{frag},1} \neq t_{\text{frag},2}$

A logical conclusion from Scenario II to explain the different densities as calculated from the distances of AB versus AC or BC (which are similar) is that  $t_{\text{frag},1} \neq t_{\text{frag},2}$ . As densities of AB are higher by about a factor 6, it is likely that at  $t_{\text{frag},1}$  there was a fragmentation of core AB and core C, while the fragmentation of cores A and B happened at a later time,  $t_{\text{frag},2}$ , following the higher density reached in AB as collapse continued after  $t_{\text{frag},1}$ . However, if one tries to calculate the masses needed of A and B separately to account for the distance of AB, we arrive at a mass of  $0.3 M_{\odot}$  of each, lower than the total

mass of core AB, which is not possible as this would suggest that core AB would have to be formed before C and AB were formed from ABC. However, this was ruled out in an isothermal collapse due to the much higher densities needed to split A and B than to form C.

4.3.4. *Scenario IV: pseudo-Isothermal collapse,  $\Lambda_{\text{now}} = \Lambda_{\text{frag,X}}$ ,  $t_{\text{frag,1}} \neq t_{\text{frag,2}}$ , Global Mass accretion*

This scenario is identical up to and some time after  $t_{\text{frag,1}}$  as Scenario III. However, due to the contradiction on the masses of AB versus the masses of A and B individually in Scenario III, a change is introduced. Even a slight drop in temperature from 20 K to 16 K in core AB is enough to obtain the conditions for the Jeans mass of  $0.35 M_{\odot}$  of A and B, as we found AB to be  $0.7 M_{\odot}$ . It is well-known the protostellar cores are generally colder in the inside as they self-shield. If accretion is going on onto AB between  $t_{\text{frag,1}}$  and  $t_{\text{frag,2}}$  the temperature is slightly lower (14 K). Such cooling lies well into the realm of possibilities as many protostellar cores show a colder inner region. See e.g. ? on B68.

4.3.5. *Scenario V: complete Isothermal collapse ( $T = 13$  K),  $\Lambda_{\text{now}} = \Lambda_{\text{frag,X}}$ ,  $t_{\text{frag,1}} \sim t_{\text{frag,2}}$ , Global Mass accretion*

It is possible to find a temperature at which the AB and C fragment and in which the core AB is again unstable at  $t_{\text{frag,1}}$  and fragments almost immediately into A and B. This is found at 13 K. However, then the masses at which the fragmentation takes place are substantially smaller ( $<0.5 M_{\odot}$  for core C and AB). Similarly the densities are also almost a factor 2 smaller. Temperatures of IRDCs and protostellar cores at low density are **XXXX argument about temperatures of IRDCs and protostellar cores with reference XXX**

4.3.6. *Caveats*

Several caveats cannot be ignored. First, a mini-cluster is formed in three dimensions and not in two. As such the observed distance,  $\Lambda$  is a projected distance and not a physical distance. The projection effects between AB, BC and AC can of course be different. **XXXX needs more XXXX**

Another big caveat is the temperature assumption of 20 K. As Scenario V shows, lower initial temperatures have a large influence: the densities needed for the observed jeans lengths are even lower, masses of the cores become very small and fragmentation should happen very quickly. **XXXX needs more XXXX**

Lastly cores can move after formation. In this case  $\Lambda_{\text{now}} \neq \Lambda_{\text{frag,X}}$ . A limit on this effect can be placed from the  $V_{\text{LSR}}$  between A, B and C. There is a small difference of at most  $0.2 \text{ km s}^{-1}$  of C and AB, while there is no detectable difference  $<0.1 \text{ km s}^{-1}$  between A and B. If one assumes a time of 0.1 Myr between  $t_{\text{frag,1}}$  and  $t_{\text{now}}$ , Core C could have moved at most 4,000 AU. However, an effect of this move would have been a higher density at which core C would have formed.

For a more thorough discussion on caveats, see Longmore (2010). **XXXX needs more XXXX**

4.3.7. *Proposed Scenario*

**XXX Make cartoon figure with time, T, and mass XXX**

Using all our available information, we propose a following scenario. The original core of NGC 2071, ABC, collapsed isothermally until reaching a critical density of  $\sim 10^5$  at the center region ( $\sim 6,000 \text{ AU}$ ) at  $t_{\text{frag,1}}$  and fragmented in cores AB and C (Scenario III) with the observed lengths. After  $t_{\text{frag,1}}$ , both AB and C begin to cool and form protostellar cores. Global accretion rates are still low as compared to the fragmentation timescales, thus deviating from iso-thermal collapse. At  $t_{\text{frag,2}}$ , AB fragments in A and B due to cooling of the cores. C does not fragment as it is smaller than the Jeans length. Depending on i) the temperature of isothermal collapse as well as ii) the cooling times between the temperature of isothermal collapse to  $T_{\text{frag,2}}$ , the time between  $t_{\text{frag,1}}$  and  $t_{\text{frag,2}}$  varies, but is significantly shorter than the accretion timescale in which cores double their mass **XXX needs ref XXX**. After  $t_{\text{frag,2}}$ , A, B and C accrete individually from the global mass reserve coming in from larger scales and form protostars.

Several facts can be concluded:

1. Mass accretion onto cores A, B and C from a global mass reservoir has to have happened and is likely still occurring. It is impossible to have fragmented into three cores with masses now observed.
2. At commonly observed temperatures of protostellar cores and IRDCs of  $\sim 20 \text{ K}$ , fragmentation will have happened at densities of  $\sim 10^5 \text{ cm}^{-2}$ .
3. Deviation from commonly observed large-scale temperatures must have occurred, either through cooling after  $t_{\text{frag,1}}$  in protostellar cores AB and C. A deviation of isothermal collapse before  $t_{\text{frag,1}}$  in core ABC to form A,B and C simultaneously is less likely as the densities from the Jeans lengths differ with a factor 7-10, indicative of different times.
4. Two fragmentation events are likely to have occurred. A first event in which C and AB were created, and second in which AB fragments into A and B. The time between these events likely depends on the cooling efficiency in protostellar cores.

more?? **XXX**

4.3.8. *Why did L1641 not fragment?*

4.4. *Relative age determination*

Although determining absolute evolutionary timescales and exact ages is very difficult for embedded sources(?), the standard model of star formation (Lada 1987; André et al. 1993; Robitaille et al. 2007; Evans et al. 2009) for low-mass sources does assume a clear evolution that can be traced in relative disk, envelope and stellar mass of an object. See e.g. Crapsi et al. (2008) for a discussion. This is confirmed by examination of model grid of Robitaille et al. (2006) and the observational results from Evans et al. (2009). Although we cannot determine absolute ages for the embedded sources,

The ratio of  $M_{\text{env}}/M_{\text{stellar}}$  is much lower in L1641 S3 MMS 1 than in any of the 2071 sources. This is indicative that L1641 S3 MMS 1 is much older. NGC 2071-C is likely the oldest source in 2071 core and began collapse after fragmentation into the supercore AB and core C. Cores A and B fragmented later, and are likely younger than C ( $M_{\text{env}}/M_{\text{stellar}}$  is equal for A and B but much higher than C)

**XXX needs extended XXX**

x

5.1. *CO isotopologues*

The chosen correlator configuration for the compact configuration observations allowed for simultaneous observations of  $C^{18}O$ ,  $^{13}CO$  and the main isotopologue of CO,  $^{12}CO$  at 219.55, 220.395 and 230.538 GHz respectively, all in their  $J=2-1$  transition.

Fig. 6 and 7 shows the outflowing gas as traced by the CO 2-1 red and blue line wings. For 2071, a complex system of flows is seen. The most clearest flow is located east-west, likely originating from 2071-A, while the a smaller second flow was found north-south, clearly originating from 2071-B. However, if one examines the channelmaps (see Fig. 9) a high velocity (with velocities higher than  $10 \text{ km s}^{-1}$  w.r.t. the source velocity) flow is seen from north-east to south-west. Large-scale observations such as ? previously identified this outflow in a NE-SW direction. It is well-known that binary interactions cause precessing outflows (?). However, that scenario is often used in close binaries. Continuum observations of the circumstellar disks with the eSMA constrain close binaries to  $<80 \text{ AU}$  and likely smaller as the disks do not deviate from classical disk shapes.

For L1641 S3 MMS 1 we identify a flow in the NE to SW direction using 7 and 8. However, the distribution of the flow is surprising. Red and blue wings emit along both directions. Red and blue high velocity components ( $> 10 \text{ km s}^{-1}$ ) are seen in both directions. In both cases, moderate velocity outflowing material encompasses these high velocity components in a "butterfly" configuration. XXX other outflow studies XXX A possible explanation is that we are looking at this outflow in the plane in the sky with the distribution of velocities caused by the turbulent shocks. However, such flows often do not show the high velocity components.

**Fig. XXX shows a PV diagram along the three outflow directions. XXX PV-diagram XXX**

$C^{18}O$  and  $^{13}CO$  are not seen in any of the outflow wings in either source. Using the limits of  $C^{18}O$ , this indicates that the wings have a relatively low optical depth  $<2.5$  across its entire wing.

5.2. *Other molecules*

With a 4 GHz bandwidth mode, a total of 8 GHz (upper and lower sideband) were obtained within a single setting at the SMA. Besides an increase in sensitivity for continuum purposes, this allows one to observe more lines near the targetted CO lines. Table 5.1 shows all identified lines at three positions (L1641, 2071-A, 2071-B). Although the main targetted lines are the CO 2-1 isotopologues, several S-bearing molecules were detected, such as OCS and SO, of which maps can be found in Fig. 11, as well as a large number of complex organics, such as methanol and formaldehyde, whose maps are shown in Figs. 12 and 13. A sample of other molecules, including several N-bearing molecules, are shown in Fig. 14. No lines were detected in the eSMA setting for NGC 2071. With a few exceptions, the position at which these lines peak are located within  $<1''$  of a continuum peak. For most lines, the agreement in line and continuum peak is much better. What is surprising is that all three main sources (NGC 2071A, B and L1641 S3 MMS 1) show very

different excitation characteristics. We discuss the complex organic emission within the scope of a central hot core and using a geometry influenced scenario in § 5.1

A good example is the methylcyanide detection. This molecule has shows a group of transitions around their  $J$  transition, corresponding to  $k-k$  quantum transitions. Close to 220 GHz, the ladder of  $J=12$  to 11 can be found. Figure 10 shows the methylcyanide,  $CH_3CN$ , spectra, around 220.7 GHz. L1641 S3 MMS 1 shows much brighter lines, as well as higher  $k$  transitions, whose detection often points to higher temperatures.

L1641 S3 MMS 1 shows by far the most detected molecules, even some of the so-called hot core molecules such as  $C_2H_5OH$  and  $NH_2CHO$ .

## 6. SPECTROSCOPIC ANALYSIS

6.0.1. *OCS*

Within the bandwidth observed, we observe two OCS transitions: 19-18 and 18-17. OCS is a linear molecule with a clearly defined ladder, similar to CO (Green & Chapman 1978), but more prominent at higher densities and temperatures. The ratio of the two transitions of this molecule can be used to give a first constraint on the excitation, using a non-LTE code, without resorting to dimensions. Such an analysis can be done most efficiently for CO and other linear molecules using the RADEX package, see e.g. the appendix in van der Tak et al. (2007). The ratio of 19-18/18-17 for 2071-A and B are 0.34 and 1.12, while the ratio of these lines are L1641 S3 MMS 1 is 0.63. Fig. XXX shows the ratio's

**XXX make OCS figure and three ratio lines XXX**

6.1. *Methylcyanide*

$CH_3CN$  has long been used in star formation as a first gage for the rotation temperature (e.g. Loren & Mundy 1984). A traditional method is to use the population diagram analysis method as detailed in Goldsmith & Langer (1999). This analysis can be found in Fig. 15. Fits are reasonably well constrained to a single population, with rotational temperatures of 145 K for L1641, and 92 K and 184 K for Peak A and Peak B. However, the rotational temperatures from NGC 2071-A and B are constrained by only 2 or 3 data points. Both  $k=0$  and 1 are either omitted or used as upper limits only, as these transitions are blended within the chosen resolution.

**A similar method using the XCLASS superset (?), provides XXX different temperatures.**

All derived temperatures are equal to kinetic temperature if one assumes the molecular gas to be in LTE and optically thin. The second assumption is likely, as the abundance of  $CH_3CN$  is often low, with typical values of a few times  $10^{-8}$  w.r.t. to  $H_2$  in hot cores (Bisschop et al. 2007). A full non-LTE RT analysis would be needed, but the uncertainty of the collisional rates are too large for the wide range of temperatures seen in the warm gas in the inner region of protostars. However, one can use the methods above to discern trends within abundances.

Bisschop et al. (2008) used the same 12-11 ladder of  $CH_3CN$  to derive rotational temperatures for IRAS 16293-2422, a  $30 L_{\odot}$  low-mass protostar in Ophiuchus. They find much higher temperatures: 370 K for 16293-2422 A and 390 K for source B. This is often interpreted

TABLE 6  
LINES DETECTED IN THE COMPACT CONFIGURATION

Molecule	Transition	Rest Freq	XXX $T_{\text{ex}}$ (K)	Chunk	2071-A	2071-B	L1641
$^{13}\text{CN}$	2-1	217.64	3.6	s47	-/-	-/-	1.26/0.23
$\text{CH}_3\text{OH}$	20 <sub>1,0</sub> -20 <sub>0,0</sub>	217.886	346.1	S44	-/-	-/-	2.75/0.42
$\text{H}_2\text{CO}$	3 <sub>0,3</sub> -2 <sub>0,2</sub>	218.222	7.3	S40	5.96/1.17	5.33/1.11	9.65/1.58
$\text{CH}_3\text{OH}$	4 <sub>2,0</sub> -3 <sub>1,0</sub>	218.440	24.3	S37	1.87/0.34	1.88/0.34	5.47/0.87
$\text{NH}_2\text{CHO}$	10 <sub>1,9</sub> -9 <sub>1,8</sub>	218.46	35.0	S37	-/-	-/-	1.63/0.30
$\text{H}_2\text{CO}$	3 <sub>2,2</sub> -2 <sub>2,1</sub>	218.475	40.0	S37	3.74/0.65	3.73/0.65	5.76/0.93
$\text{H}_2\text{CO}$	3 <sub>2,1</sub> -2 <sub>2,0</sub>	218.762	40.0	S33	4.05/0.77	3.63/0.73	6.01/1.01
$\text{H}_2^{13}\text{CO}^b$	10 <sub>2,9</sub> -9 <sub>2,8</sub>	218.820	42.7	S32	2.76/0.27	1.68/0.22	-/-
OCS	18-17	218.903	62.1	S32/31	6.73/0.53	3.91/0.45	3.75/0.55
$\text{HCOOH}^b$	8 <sub>1,8</sub> -7 <sub>0,7</sub>	218.935	20.9		3.94/0.19	-/-	-/-
$\text{C}^{18}\text{O}$	2-1	219.555	3.67	S24	3.12/1.21	-/-	2.45/0.77
$\text{HNCO}$	10-9	219.805	33.0	S21	-/-	-/-	2.42/0.36
$\text{H}_2^{13}\text{CO}$	3 <sub>1,2</sub> -2 <sub>2,1</sub>	219.910	15.6	S20	0.58/0.16	-/-	2.08/0.3
SO	5-4	219.950	17.0	S19	4.23/1.15	12.77/1.66	5.10/1.09
$\text{CH}_3\text{OH}$	8 <sub>0,0</sub> -7 <sub>1,0</sub>	220.078	59.8	S18/S17	-/-	-/-	3.22/0.6
$^{13}\text{CO}$	2-1	220.395	3.7	S14/S13			
$\text{HNCO}$	10 <sub>1,9</sub> -9 <sub>1,8</sub>	220.585	63.2		-/-	-/-	1.22/0.20
$\text{CH}_3\text{CN}$	12 <sub>6</sub> -11 <sub>6</sub>	220.594	219.2		-/-	0.96/0.14	1.01/0.26
$\text{CH}_3\text{CN}$	12 <sub>5</sub> -11 <sub>5</sub>	220.641	164.6		-/-	-/-	1.19/0.33
$\text{CH}_3\text{CN}$	12 <sub>4</sub> -11 <sub>4</sub>	220.679	119.9		-/-	-/-	1.75/0.40
$\text{CH}_3\text{CN}$	12 <sub>3</sub> -11 <sub>3</sub>	220.709	85.2		1.02/0.24	1.75/0.29	1.62/0.47
$\text{HO}_2^b$	3 <sub>1,2</sub> -2 <sub>1,1</sub>	220.720	25.5		-/-	-/-	1.80/0.40
$\text{CH}_3\text{CN}^a$	12 <sub>2</sub> -11 <sub>2</sub>	220.730	60.3		-/-	-/-	-/-
$\text{CH}_3\text{CN}^c$	12 <sub>1</sub> -11 <sub>1</sub>	220.743	45.		1.90/0.27	2.23/0.25	4.77/0.67
$\text{CH}_3\text{CN}^c$	12 <sub>0</sub> -11 <sub>0</sub>	220.747	40.5		1.90/0.27	2.23/0.25	4.77/0.67
Upper sideband							
$\text{CH}_3\text{OH}$	15 <sub>4,0</sub> -16 <sub>3,0</sub>	229.589	252.6	S01/02	-/-	-/-	4.15/0.54
$\text{CH}_3\text{OH}$	8 <sub>-1,0</sub> -7 <sub>0,0</sub>	229.758	54.3	S03/04	2.17/0.67	4.68/0.55	6.60/1.26
$\text{CH}_3\text{CHO}$	10 <sub>3,7</sub> -10 <sub>2,8</sub>	229.860	41.9	S05	-/-	-/-	2.16/0.51
$\text{CH}_3\text{OH}$	19 <sub>5,0</sub> -20 <sub>4,0</sub>	229.864	394.5	S05	-/-	-/-	1.60/0.36
$\text{CH}_3\text{OH}$	3 <sub>-2,0</sub> -4 <sub>-1,0</sub>	230.027	20.0	S07	1.54/0.26	-/-	3.62/0.60
$^{12}\text{CO}$	2-1	230.538	3.5	S14			
OCS	19-18	231.065	69.4	S19/S20	2.30/0.78	4.4/0.60	2.36/0.53
$\text{CH}_3\text{OH}$	10 <sub>2,0</sub> -9 <sub>3,0</sub>	231.281	107.2	S23	-/-	1.07/0.21	3.32/0.63
$\text{CH}_3\text{CHO}$	12 <sub>3,9</sub> -11 <sub>3,8</sub>	231.968	56.64	S30	-/-	-/-	3.56/0.52
$\text{C}_2\text{H}_5\text{OH}$	17 <sub>5,13</sub> -17 <sub>4,14</sub>	232.404	107.4	S36	-/-	-/-	3.42/0.61
$\text{CH}_3\text{OH}$	10 <sub>2,0</sub> -9 <sub>3,0</sub>	232.418	107.2	S36	1.84/0.20	2.25/0.22	5.79/0.62
$\text{CH}_3\text{OH}$	18 <sub>3,0</sub> -17 <sub>4,0</sub>	232.783	302.6	S40	-/-	-/-	2.26/0.40
$\text{CH}_3\text{OH}$	10 <sub>-3,0</sub> -11 <sub>-2,0</sub>	232.945	124.5	S42	-/-	2.02/0.2	3.25/0.56
$\text{C}_2\text{H}_5\text{OH}$	15 <sub>5,11</sub> -15 <sub>4,12</sub>	233.215	84.2	S45	-/-	-/-	2.99/0.24

<sup>a</sup> line is detected. However, as it was at the edge of two chunks, no reliable fluxes or peak fluxes could be extracted.

<sup>b</sup> uncertain identification

<sup>c</sup> Lines blended

TABLE 7  
ROTATIONAL TEMPERATURES, COLUMN DENSITIES AND ABUNDANCES OF DETECTED MOLECULES

Source	$\text{CH}_3\text{OH}$	$\text{H}_2\text{CO}$	$\text{CH}_3\text{CN}$	$\text{CH}_3\text{CHO}$	$\text{C}_2\text{H}_5\text{OH}$
Rotational temperatures (K)					
2071-A			92		
2071-B			184		
L1641	230		145		
Column density ( $\text{cm}^{-2}$ )					
2071-A					
2071-B					
L1641					
Abundance w.r.t $\text{H}_2$					
2071-A					
2071-B					
L1641					

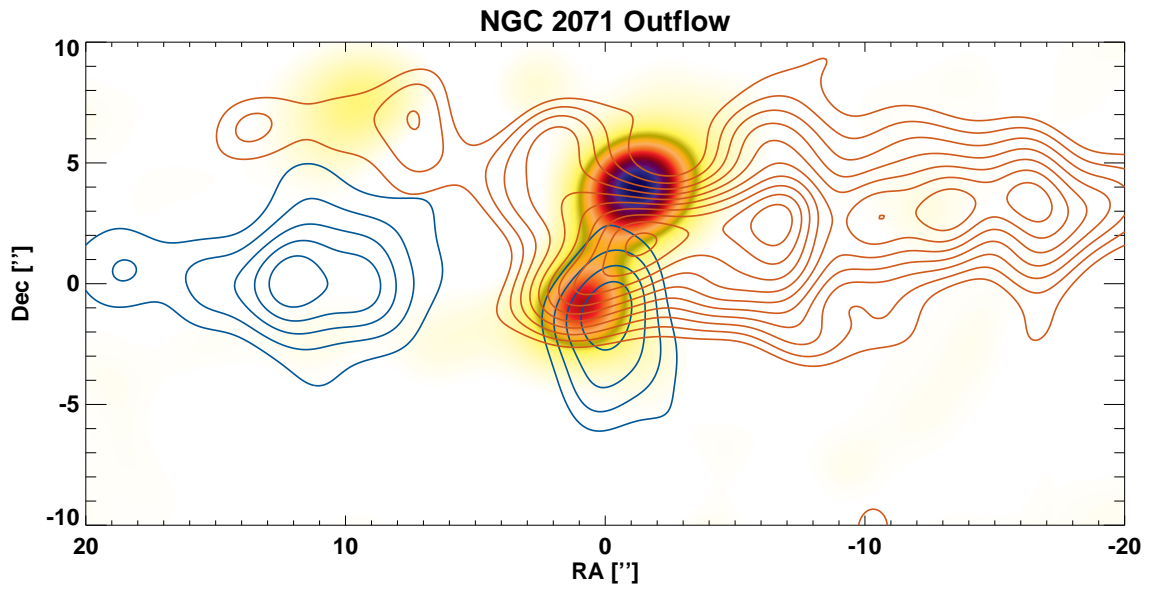


FIG. 6.— NGC2071 Outflows as traced by the CO line wings in *blue* ( $-6$  to  $-2.5$   $\text{km s}^{-1}$  w.r.t.  $V_{\text{LSR}}$ ) and *red* ( $+2.5$  to  $+6$  w.r.t.  $V_{\text{LSR}}$ ).

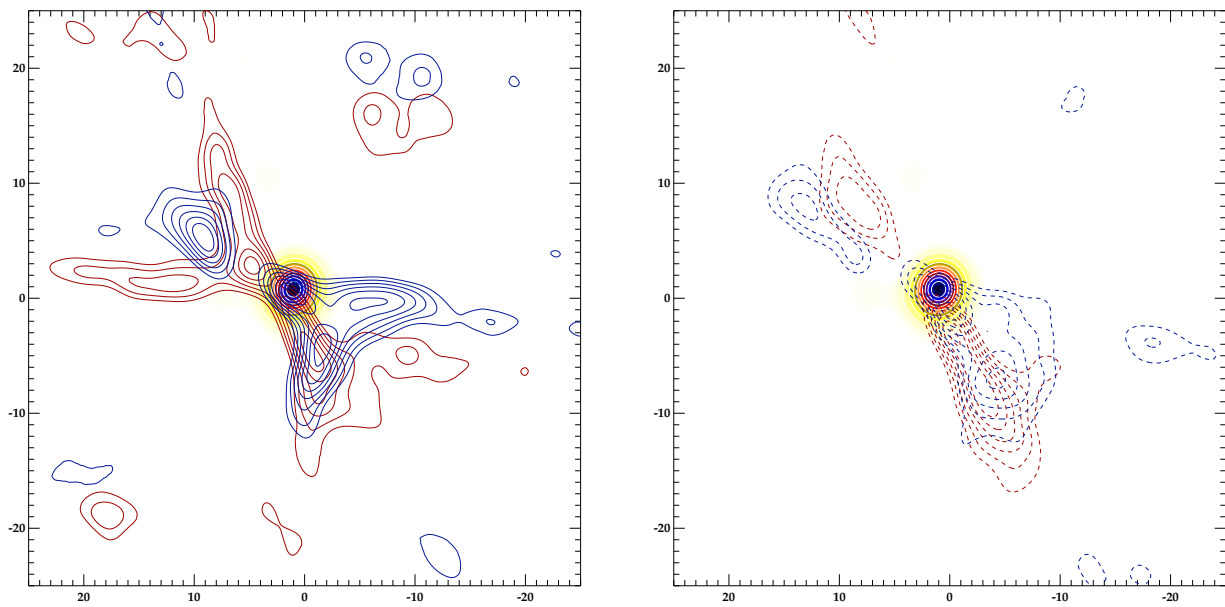


FIG. 7.— Moderate and Extreme velocities around L1641, clearly showing the "butterfly" effect of the L1641 outflow in which the extreme velocity emission is 'encapsulated' around more moderate velocities

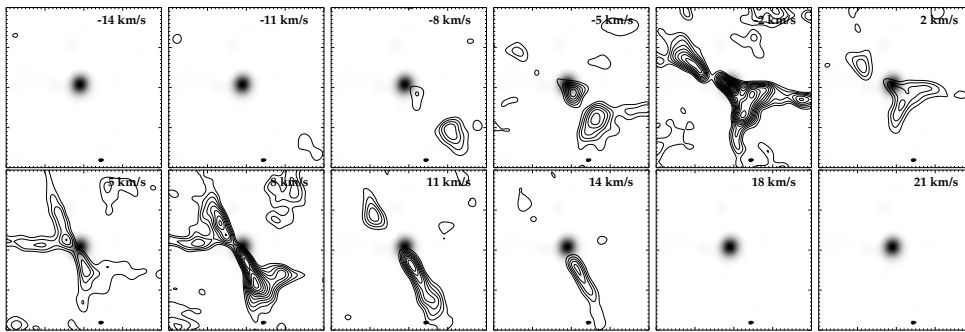


FIG. 8.— Channel map of the L1641 outflow as traced by CO 2-1

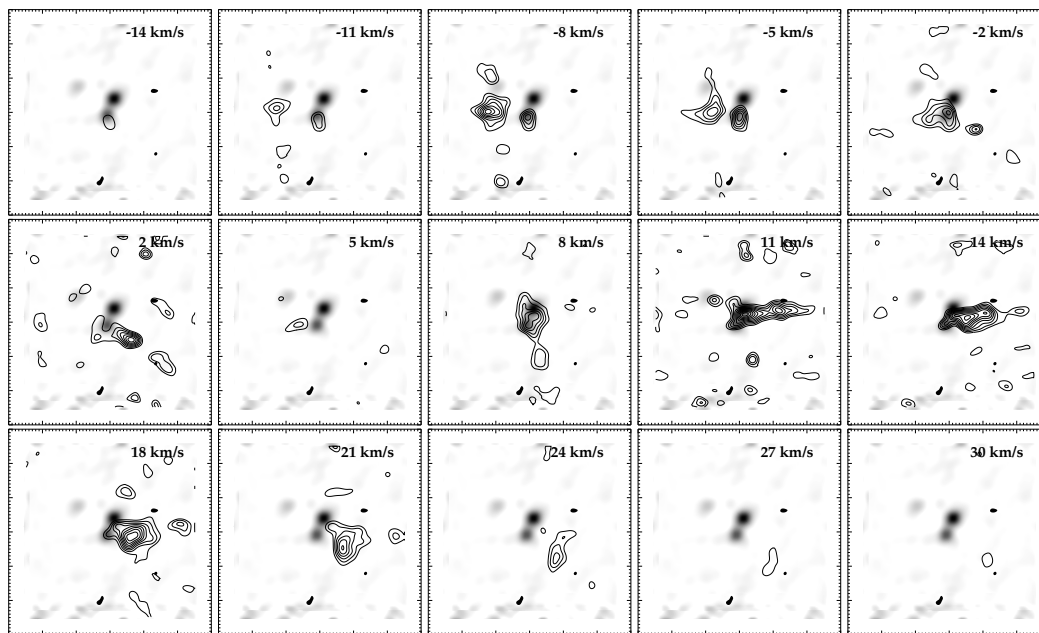


FIG. 9.— Channel map of the NGC 2071 outflows as traced by CO 2-1

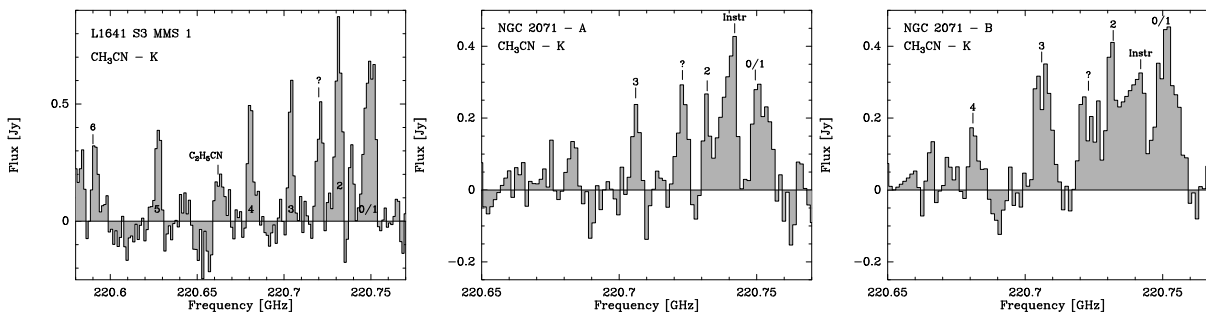


FIG. 10.— Spectra of the detected  $\text{CH}_3\text{CN}$  12-11 ladder around 220.7 GHz.

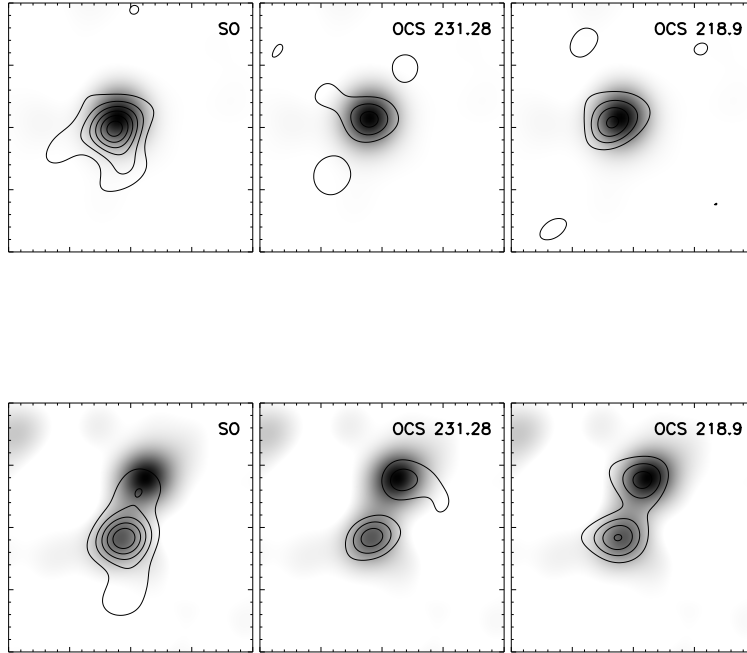


FIG. 11.— Maps of integrated flux of S-bearing molecules of L1641 (top) and NGC 2071 (bottom)

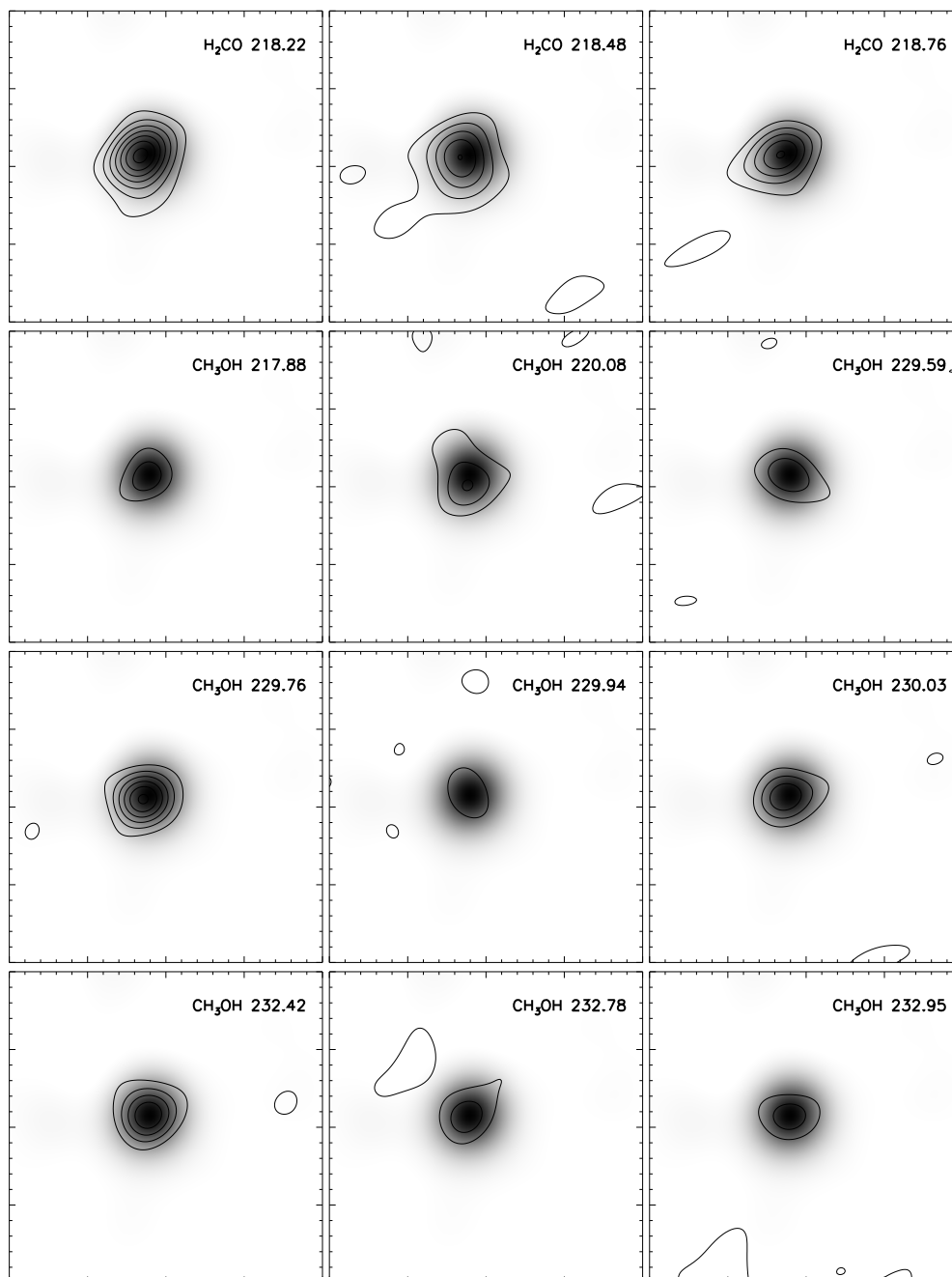


FIG. 12.— Maps of integrated flux of methanol and formaldehyde of L1641.

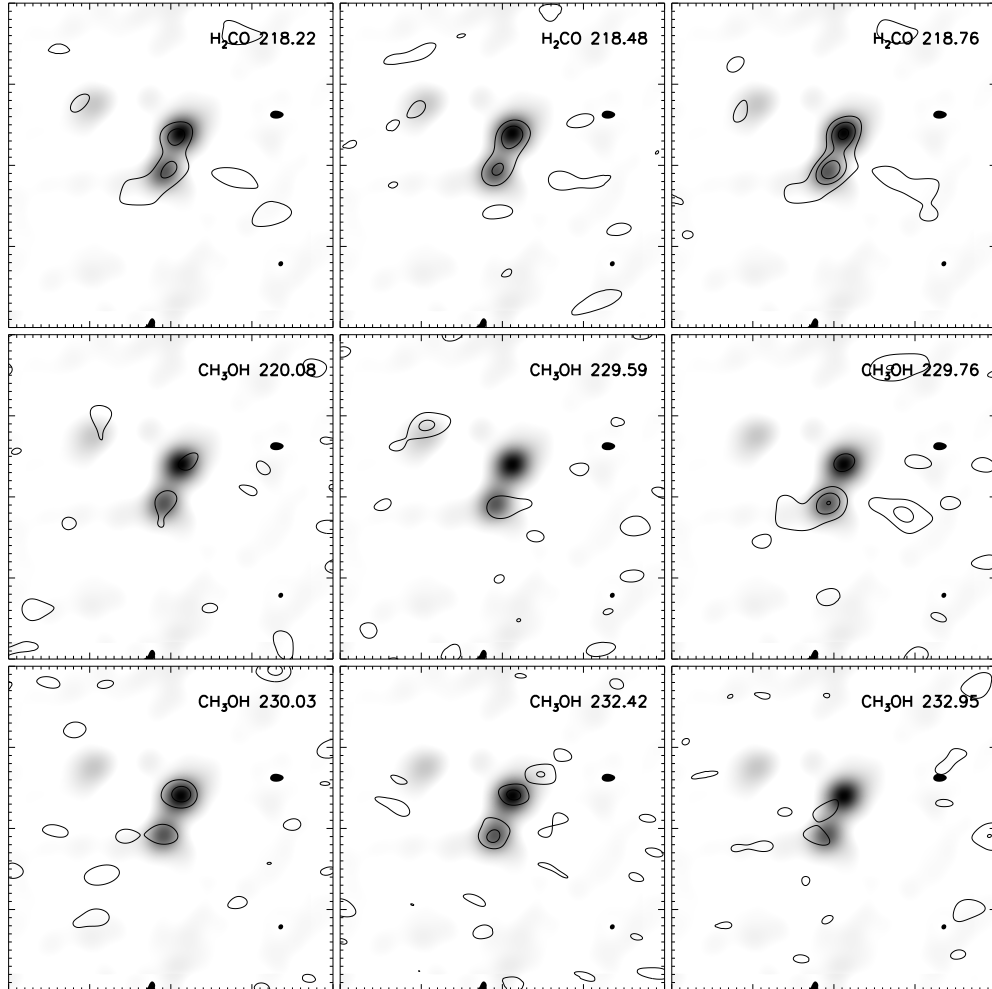


FIG. 13.— Maps of integrated flux of methanol and formaldehyde of NGC 2071.

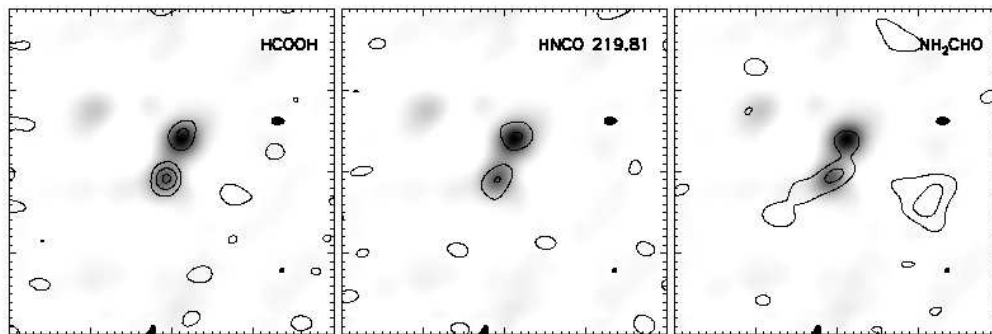
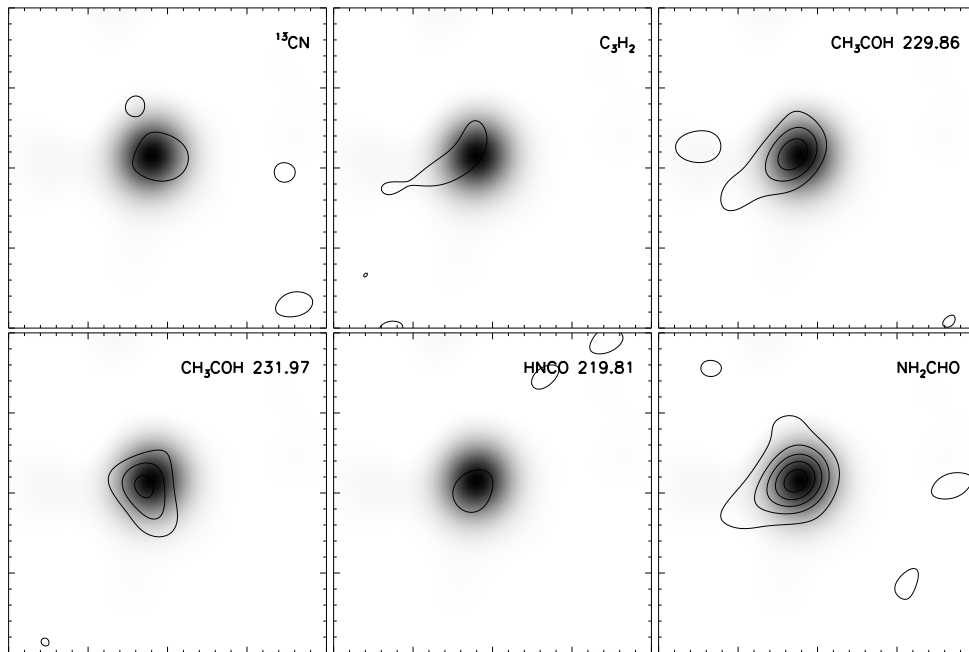


FIG. 14.— Maps of integrated flux of the other molecules of L1641 (top) and NGC 2071 (bottom).

as a “hot corino”, but Bisschop et al. (2008) propose XXX

A similar analysis, done in Bisschop et al. (2007), surveyed seven high-mass hot cores. Rotational temperatures between 170 and almost 300 K were found. This is indicative of relatively “colder”  $\text{CH}_3\text{CN}$  due to the increased area.

The results from NGC 2071 and L1641 S3 MMS 1 seem to be a type of source that has a true hot core like chemistry, following the temperatures from Bisschop et al. (2008). Low-mass protostars commonly have fewer detected lines due to a much smaller emitting area but higher rotational temperatures.

## 6.2. $\text{CH}_3\text{OH}$ and $\text{H}_2\text{CO}$

The presence of the basic complex organics, methanol and formaldehyde, has often been interpreted as a first step to the presence of a hot core, or in the case of lower mass protostars, a hot corino. However recent studies, such as Bisschop et al. (2007), Bisschop et al. (2008), Jørgensen et al. (2005), Kristensen et al. (2010) shows that the picture may be different and that either gas-grain chemistry and corresponding interactions may be of prime importance, or that non-dissociative C-shocks dominate in the excitation. Only in some high-mass protostars a hot core is created solely through gas-phase chemistry.

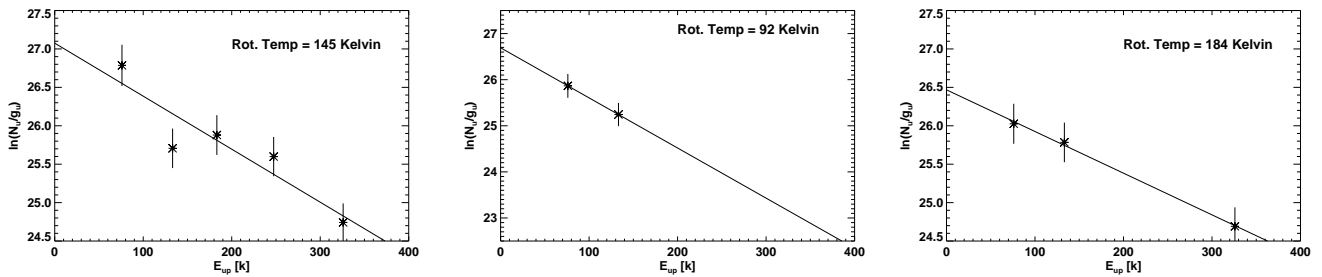


FIG. 15.—  $\text{CH}_3\text{CN}$  population diagrams with fitted rotational temperature. L1641 (left, peak A (middle) and peak B (right))

When we examine our IM protostars within such a scope, it can be seen that the complex organics of peak A and peak B are much weaker than the ones seen at the position L1641 S3 MMS1. This is in contrast with the CO isotopologues, which are stronger for NGC 2071. A likely cause for this is the emitting area of the lines, which might be smaller in 2071, while CO fills the beam in both sources.

Thus, a possible conclusion is that the relative amount of cold gas within the central area in and around the NGC 2071 protocluster is much larger than around L1641 S3 MMS 1.

Similarly, if all methanol is optically thin, more warm gas must exist around L1641 S3 MMS 1. If one assumes the sources are at similar distances ( $\sim 450$  pc), this has severe consequences for the physical origin. L1641 S3 MMS 1 has to have a more powerful source of energy to excite these complex organics, such as higher accretion rates, a more massive central protostar or more powerful shocks. However, without considering the full excitation, including non-LTE and temperature gradients effects, one cannot conclusively pin this down to a single characteristic yet. From our SED and dust analysis, we did in fact determine that the stellar mass of L1641 S3 MMS 1 is a factor 3-4 larger than for NGC 2071. Assuming a fully evolved star, such star do produce XXX % more UV radiation due to the higher surface temperature. However, accretion onto lower-mass protostars can still dominate the total UV production at these embedded stages.

If one applies the population diagram analysis from Goldsmith & Langer (1999) to the detected complex organic molecules of methanol, one can probe into the excitation mechanisms of the central region, similar to the analysis of OCS done earlier. One has to assume LTE and isothermality to derive column densities, as well as adopt an optically thin limit. For methanol, L1641 shows a rotational temperature of 230 K, higher to what is found for the  $\text{CH}_3\text{CN}$ , but similar to the rotational temperatures of methanol of hot cores in Bisschop et al. (2007).

At these scales, most low-mass sources do not show any methanol lines, even in the  $7_k - 6_k$  ladder, see e.g. the PROSAC survey of Jørgensen et al. (2007). There, with the exception of NGC 1333 IRAS 2A, all detected methanol lines were clearly detected significantly off-source ( $> 2100$  AU). Even with the increased distance of Orion vs. Perseus (450 vs 300 pc), any similar outflow emission associated with 2071 or L1641 would still have been seen off-source.

Sadly, the distribution of methanol lines as function of

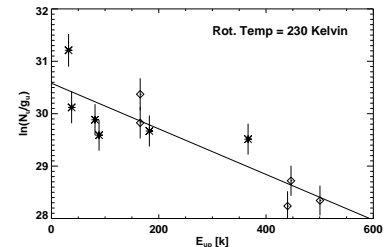


FIG. 16.— Methanol population diagrams with fitted rotational temperature of L1641

excitation energy for NGC 2071-A and 2071-B was not good enough to reliably derive a rotational temperature, a common feature for these lines in low-mass protostars. This lack of detection of higher excitation energies would be indicative of a small hot core.

The rotational temperature derived for the methanol in the hot core around NGC 7129 FIRS 2 (Fuente et al. 2005a) is much higher (809 K), although the coverage of energies is much lower ( $E_{\text{up}} < 150$  K). If we fit only our lines with a similar coverage as was done in Fuente et al. (2005a), a rotational temperature  $< 350$  K is obtained as an upper limit for L1641 S3 MMS 1.

**XXX calculate column densities and abundances XXX**

**XXX H<sub>2</sub>CO optically thick? XX**

**XXX ethanol, CH<sub>3</sub>CHO rot temp XX**

## 7. THE INFLUENCE OF FRAGMENTATION AND STRUCTURE ON THE CHEMISTRY OF IM PROTOSTARS AND MINI-CLUSTERS

At small scales, it is shown that emission from complex molecules around low-mass proto-stars Jørgensen et al. (e.g. 2007), is almost uniquely tied to outflowing material. Only a select few (e.g. IRAS 16293-2422, NGC 1333 IRAS 2A) show emission of complex species, both organic and S-bearing, associated with the continuum peak. note that these select few often have luminosities on the high end of what one considers low-mass. New studies at high frequencies of e.g. CO 6-5 and 7-6 van Kempen et al. (2009c) raised the idea that in addition to outflows, the structure of the outflow cavity can be a major influence on the excitation of higher excitation molecules associated with the warm ( $T > 100$  K) gas through photon heating (Spaans et al. 1995). Due to the low density within the outflow cavity, soft-UV photons irradiate the cavity walls, heating the gas at much larger distances without needing to invoke a precarious balance

of non-dissociative C-shocks.

To determine if the protostars in our sample can sustain a hot core, we construct Dusty models using the derived luminosity, in turn calculate the sizes of spherical central region with  $T > 100$  K, assume typical hot core abundances and then predict upper limits to the flux.

**XXX DUSTY with Luminosity, calculate size of hot corino, do the abundances make sense? XXX**  
**XXX Bisschop 2007,2008 analysis XXX**

The series of papers written by S. Bruderer et al. (Stäuber et al. 2007; Bruderer et al. 2009b,a, 2010) demonstrate that the introduction of a outflow cavity has large impact on the chemistry driven by UV in high-mass sources and low-mass sources. Observationally, more evidence has been published with recent Herschel and APEX Champ+ results (van Kempen et al. 2009b, 2010; Kristensen et al. 2010) that XXXX.

## 8. CONCLUSIONS

In this paper, we presented a dataset on two IM protostellar cores: L1641 S3 MMS 1 and NGC 2071. The conclusions can be summed up as follows:

- Continuum observations of Spitzer and SMA at different configurations show that although at large scales these two sources are similar in mass ( $\sim 25 M_{\odot}$ ), NGC 2071 has fragmented into three protostars. All three protostars are deeply embedded, similar to the Stage 0 sources as defined by the classification of Evans et al. (2009). Masses of the NGC 2071 fragmentation has ...
- influence of accretion rate???
- chemistry of UV production??

### 8.1. Fragmentation and its impact on chemistry

The influence of fragmentation of IM protostellar cores is of vital importance in detecting lines. Sources which seem very similar on scales of  $15''$  or larger, such as NGC 2071 and L1641 S3 MMS 1, are very different at smaller scales. Single sources likely produce much more complex molecular emission, similar to the hot cores around high-mass sources. However, sources that appear to be of intermediate mass, but are in fact a small cluster of protostars with each individual star more similar to a low-mass protostar, show less complex emission. However, such a cluster cannot be treated as a sum of several isolated low-mass protostars, as turbulent heating (e.g. from outflows) can have a large influence. The time-scale at which fragmentation takes place XXX

## 9. TO DO

- Continuum modelling in UV plane??
- Position-velocity diagram of CO.
- CH<sub>3</sub>CN temperature from Keping
- rotational temperatures of all species
- Do Bisschop et al. 2007,2008 comparison

TvK and SL are supported as SMA postdoctoral fellows at the Harvard-Smithsonian Center for Astrophysics (CfA) and are thankful for the Submillimeter Array for funding their research. Mark Gurwell, Ken Young (Taco) and David Wilner are thanked for tracksharing the eSMA night. We are grateful for the WISH IM team for supplying necessary information on the sources and for extensive discussion. We appreciate the help of Tom Megeath with sharing the reduced Spitzer photometry and images on Orion before publication.

*Facilities:* SMA

## REFERENCES

- Adams, F. C. & Myers, P. C. 2001, *ApJ*, 553, 744  
 Adams, F. C., Proszkow, E. M., Fatuzzo, M., & Myers, P. C. 2006, *ApJ*, 641, 504  
 André, P., Ward-Thompson, D., & Barsony, M. 1993, *ApJ*, 406, 122  
 Beltrán, M. T., Estalella, R., Girart, J. M., Ho, P. T. P., & Anglada, G. 2008, *A&A*, 481, 93  
 Bisschop, S. E., Jørgensen, J. K., Bourke, T. L., Bottinelli, S., & van Dishoeck, E. F. 2008, *A&A*, 488, 959  
 Bisschop, S. E., Jørgensen, J. K., van Dishoeck, E. F., & de Wachter, E. B. M. 2007, *A&A*, 465, 913  
 Bruderer, S., Benz, A. O., Bourke, T. L., & Doty, S. D. 2009a, *A&A*, 503, L13  
 Bruderer, S., Benz, A. O., Doty, S. D., van Dishoeck, E. F., & Bourke, T. L. 2009b, *ApJ*, 700, 872  
 Bruderer, S., Benz, A. O., Stäuber, P., & Doty, S. D. 2010, *ArXiv e-prints*  
 Crapsi, A., van Dishoeck, E. F., Hogerheijde, M. R., Pontoppidan, K. M., & Dullemond, C. P. 2008, *ArXiv e-prints*, 801  
 Di Francesco, J., Johnstone, D., Kirk, H., MacKenzie, T., & Ledwosinska, E. 2008, *ApJS*, 175, 277  
 Duchêne, G., Bontemps, S., Bouvier, J., et al. 2007, *A&A*, 476, 229  
 Enoch, M. L., Evans, N. J., Sargent, A. I., & Glenn, J. 2008, *ApJ*, submitted  
 Evans, II, N. J., Dunham, M. M., Jørgensen, J. K., et al. 2009, *ApJ* in press  
 Fontani, F., Zhang, Q., Caselli, P., & Bourke, T. L. 2009, *A&A*, 499, 233  
 Fuente, A., Ceccarelli, C., Neri, R., et al. 2007, *A&A*, 468, L37  
 Fuente, A., Neri, R., & Caselli, P. 2005a, *A&A*, 444, 481  
 Fuente, A., Rizzo, J. R., Caselli, P., Bachiller, R., & Henkel, C. 2005b, *A&A*, 433, 535  
 Goldsmith, P. F. & Langer, W. D. 1999, *ApJ*, 517, 209  
 Green, S. & Chapman, S. 1978, *ApJS*, 37, 169  
 Gutermuth, R. A., Megeath, S. T., Myers, P. C., et al. 2009, *ApJS*, 184, 18  
 Johnston, K., Keto, E., & Zhu, Q. 2010, in prep, 545, 327  
 Jørgensen, J. K., Bourke, T. L., Myers, P. C., et al. 2007, *ApJ*, 659, 479  
 Jørgensen, J. K., Schöier, F. L., & van Dishoeck, E. F. 2005, *A&A*, 437, 501  
 Keto, E. & Zhang, Q. 2010, *ArXiv e-prints*  
 Kristensen, L. E., Visser, R., van Dishoeck, E. F., et al. 2010, *ArXiv e-prints*  
 Lada, C. J. 1987, in *IAU Symp. 115: Star Forming Regions*, ed. M. Peimbert, J. Jugaku, & P. W. J. L. Brand (Reidel, Dordrecht), 1  
 Longmore, S., e. a. 2010, in prep  
 Loren, R. B. & Mundy, L. G. 1984, *ApJ*, 286, 232  
 Ossenkopf, V. & Henning, T. 1994, *A&A*, 291, 943  
 Robitaille, T. P., Whitney, B. A., Indebetouw, R., & Wood, K. 2007, *ApJS*, 169, 328  
 Robitaille, T. P., Whitney, B. A., Indebetouw, R., Wood, K., & Denzmore, P. 2006, *ApJS*, 167, 256  
 Shirley, Y. L., Evans, N. J., Rawlings, J. M. C., & Gregersen, E. M. 2000, *ApJS*, 131, 249

- Spaans, M., Hogerheijde, M. R., Mundy, L. G., & van Dishoeck, E. F. 1995, *ApJ*, 455, L167+
- Stäuber, P., Benz, A. O., Jørgensen, J. K., et al. 2007, *A&A*, 466, 977
- van der Tak, F. F. S., Black, J. H., Schöier, F. L., Jansen, D. J., & van Dishoeck, E. F. 2007, *A&A*, 468, 627
- van der Tak, F. F. S., van Dishoeck, E. F., Evans, N. J., Bakker, E. J., & Blake, G. A. 1999, *ApJ*, 522, 991
- van Kempen, T. A., Doty, S. D., van Dishoeck, E. F., Hogerheijde, M. R., & Jørgensen, J. K. 2008, *A&A*, 487, 975
- van Kempen, T. A., Kristensen, L. E., Herczeg, G. J., et al. 2010, *A&A*, 518, L121+
- van Kempen, T. A., van Dishoeck, E. F., Guesten, R., et al. 2009a, *ArXiv e-prints*
- van Kempen, T. A., van Dishoeck, E. F., Güsten, R., et al. 2009b, *A&A*, 501, 633
- van Kempen, T. A., van Dishoeck, E. F., Salter, D. M., et al. 2009c, *A&A*, 498, 167
- Vázquez-Semadeni, E., Gómez, G. C., Jappsen, A., Ballesteros-Paredes, J., & Klessen, R. S. 2009, *ApJ*, 707, 1023
- Zavagno, A., Molinari, S., Tommasi, E., Saraceno, P., & Griffin, M. 1997, *A&A*, 325, 685

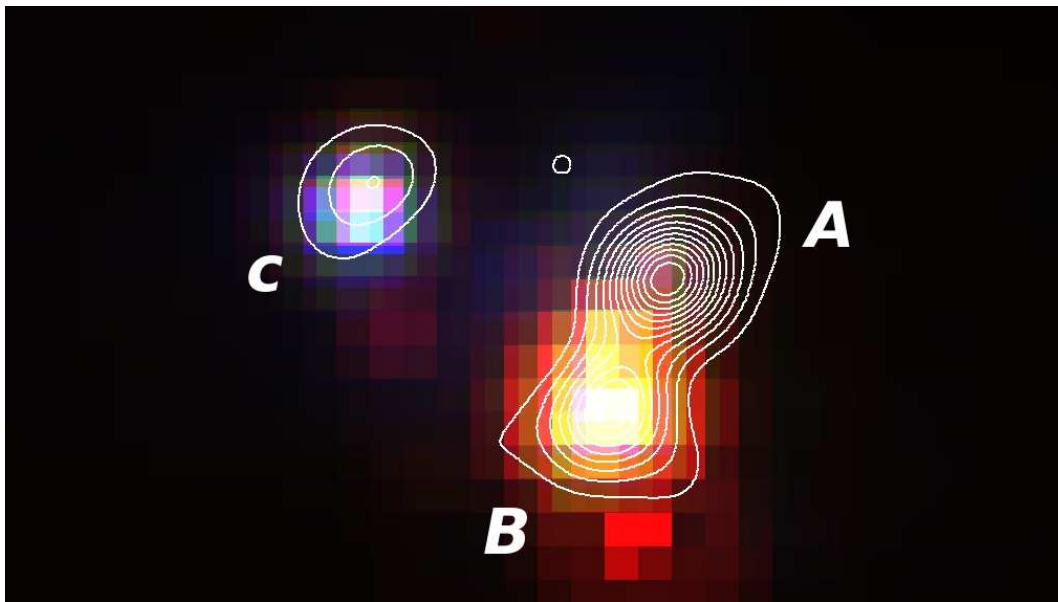


FIG. 17.— SMA continuum overplotted over the Spitzer IRAC 3.6, 5.6 and 8  $\mu\text{m}$  images

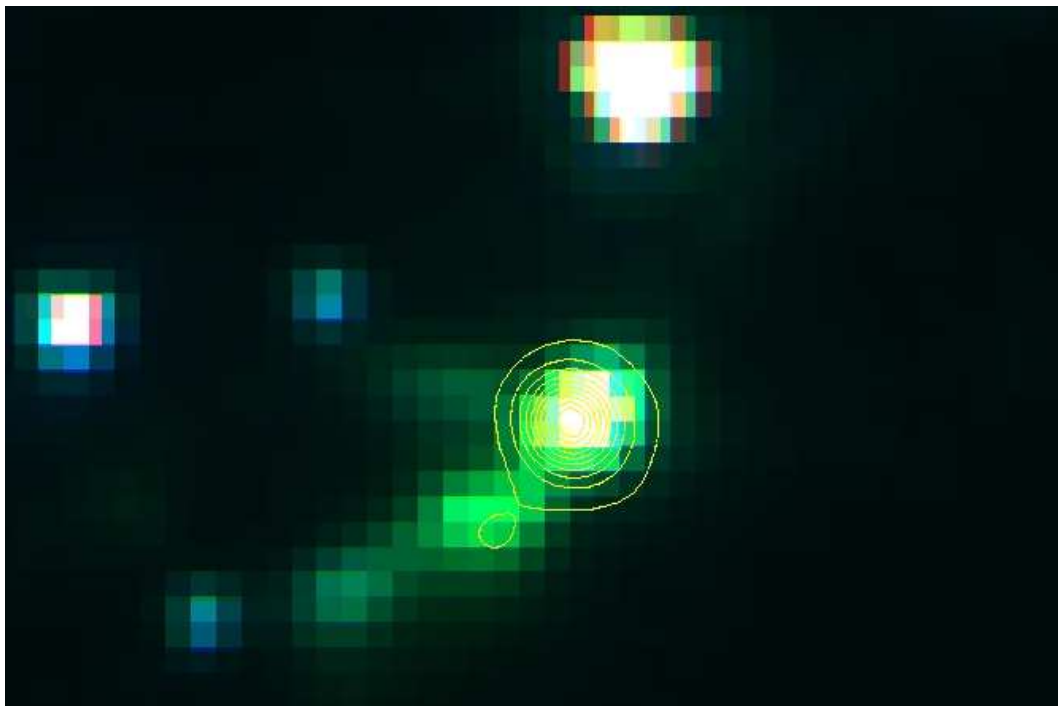


FIG. 18.— SMA continuum overplotted over the Spitzer IRAC 3.6, 5.6 and 8  $\mu\text{m}$  images of L1641 S3 MMS1

#### APPENDIX SPITZER

Within the scope of the Orion Spitzer program, NGC 2071 and L1641 S3 MMS 1 were observed using the IRAC and MIPS camera's. These will be published in a future publication led by Tom Megeath and Giovanni Fazio. Figure 17 and 18 overplot the submm interferometry on the Spitzer images. In addition, photometry was extracted from the images using Aladin and can be found in Table A, with the exception of 24 micron in NGC 2071. This position was saturated at that wavelength. **XXX needs more**

TABLE 8  
TABLE WITH SPITZER AND 2MASS PHOTOMETRY

Source	J Jy	H Jy	K Jy	IRAC 1 Jy	IRAC 2 Jy	IRAC 3	IRAC 4	MIPS 1
2071-A	1.6e-4	7.9e-4	4.6e-3	7.0e-2	4.9e-2	2.2e-1	0.9	
2071-B	3e-4	2.2e-3	2.1e-2	4.4e-2	3.7e-2	1.7e-1	0.7	-
2071-C	2.3e-3	6.0e-3	4.5e-2	8.6e-2	6.0e-2	2.7e-1	1.2	
L1641 S3 MMS 1	-	-	-	0.69	0.82	2.3	17.2	